Indian Journal of Pure & Applied Physics
Vol. 55, March 2017, pp. 198-202

Full analysis of a high-bandwidth microring-based PIN modulator

Mahmoud Nikoufard* & Masoud Kazemi Alamouti

Department of Electronics, Faculty of Electrical and Computer Engineering, University of Kashan, Kashan, Iran

Received 22 January 2016; revised 23 December 2016; accepted 29 December 2016

This study presents a new simulation strategy for a high-speed microring-based PIN modulator using the finite element method. It includes dc and transient simulations of the electro-optical behavior of the device. Variations in the effective refractive index and their effect on the optical output fields are determined by applying a reverse bias voltage pulse to the device. The frequency responses have been calculated for the microring modulator and 3 dB bandwidth. Calculations show a 3 dB bandwidth of over 115 GHz for a ring with a radius of 8 µm and a width of 0.5 µm at -7 V biasing voltage.

Keywords: Microring-based modulator, Frequency response, Electro-optic modulation, Transient analysis, InP material

1 Introduction

Modulators convert electrical data to optical data in high speed optical communications[1]. For direct modulation of injected carriers of Fabry-Perot lasers, parameters such as photon-carrier interaction, frequency chirp, and differential gains limit the modulation bandwidth[2,3]. Higher bit-rates and long optical fiber links require external modulators. Several types of external electro-optic modulators are realized based on Mach-Zehnder interferometer (MZI) and ring-resonator schemes on $LiNbO_3$[4], polymer[5], GaAs[6], and InP[7] materials. Electro-optic modulators on an InP substrate have the advantage of monolithic integration with lasers at a wavelength[8] of 1.55 µm.

Travelling wave (TW)-MZI modulators on the InP substrate are relatively large (mm range) and have the highest bandwidth of 112 Gbit/s dual polarization quadrature phase shift keying[9]. A MZI-based PIN modulator was investigated having a bandwidth of more than 40 GHz with the ability of monolithic integration with an arrayed waveguide grating laser[10]. To overcome the deficiencies in the TW-MZI, electro-optic modulators using a high-quality optical ring cavity have been proposed on polymers[11] and semiconductor-on-insulator platforms[12]. Micro-ring (MR) modulators have a natural resonance. Changing the radius and refractive index of the ring will shift the resonant wavelength and produce a large modulation depth near the resonance peak. MR modulators[11,12] have low insertion loss and driving voltage, but cannot be integrated with active components.

The present study presents and fully analyzes a novel high-speed ring resonator modulator based on carrier depletion in a reverse-biased PIN diode on an InP substrate. The simulation accounts for the electrical and optical properties of the microring PIN modulator using the finite element method (FEM).

2 Microring-Based Modulator

A schematic structure for the MR modulator is illustrated in Fig. 1(a). The structure is composed of a conventional PIN layer stack and a ring resonator which is coupled to two straight waveguides. The width of the ring and the straight waveguides, the gap between the ring and the straight waveguides, and the radius of ring are shown in Fig. 1(b). The layer stack consists of a film layer of non-intentionally doped InGaAsP with a bandgap wavelength of 1.25 µm, a thickness of 500 nm, a doping level of $6\times10^{16}/cm^3$, and an upper cladding layer of p-InP with a doping level of $10^{18}/cm^3$ and a thickness 1 µm on a highly n-doped substrate having a doping level of $10^{18}/cm^3$. The ring cavity has two additional thin layers of p^{++} and n^{++} InGaAs with a doping of $4\times10^{19}/cm^3$ as the ohmic p and n contact layers on top and an electrode on each side to apply reverse voltage (Fig. 1(c)). An optical continuous wave illuminates the input port of the straight waveguide and is coupled to the ring cavity. By applying reverse bias voltage to the electrodes, the guiding layer and part of the adjacent layers are fully depleted and the effective refractive index of the ring varies from the plasma dispersion

*Corresponding author (E-mail: mnik@kashanu.ac.ir)

effect, band filling (BF) effect, and electrical field created in the PIN junction[10]. The change in the effective refractive index of the ring waveguide modifies the resonance wavelength and subsequently modulates the transmitted signal.

An accurate three-dimensional simulation of the ring resonator modulator requires a high-speed and high-capacity computer with a long execution time. These limitations mean that the ring resonator modulator was primarily analyzed to determine the carrier concentration, electrical field, and effective refractive index in the lateral cross-section (Fig. 1(c)) and then the optical field distribution, transmission and 3-dB bandwidth in the longitudinal cross-section (Fig. 1(b)).

The free carrier concentration and the electric field inside the PIN structure vary, which changes the refractive index of the InP cladding and InGaAsP film layers by applying reverse bias voltage to the electrodes of the ring. The electro-optical effects in the bulk InP and InGaAsP are given for the Pockels, Kerr, plasma, and BF effects [10,13,14] as:

$$\Delta n_{\text{pockels}} = \pm \frac{1}{2} n_0^{\,3} r_{41} |E| \qquad \ldots(1)$$

$$\Delta n_{\text{kerr}} = \frac{1}{2} n_0^{\,3} S_{12,11} E^2 \qquad \ldots(2)$$

$$\Delta n_{\text{plasma}} = \frac{e^2 \lambda^2}{8\pi^2 c^2 \varepsilon_0 n_0} \left[\frac{N}{m_e} + P \left(\frac{m_{hh}^{1/2} + m_{lh}^{1/2}}{m_{hh}^{3/2} + m_{lh}^{3/2}} \right) \right] = A(E) N_d \qquad \ldots(3)$$

$$\Delta n_{\text{BF}} = A_{\text{BF}} N_d \qquad \ldots(4)$$

$$\Delta n_{\text{total}} = \Delta n_{\text{plasma}} + \Delta n_{\text{BF}} + \Delta n_{\text{kerr}} + \Delta n_{\text{pockels}} \qquad \ldots(5)$$

In which n_0 is the refractive index, r_{41} is the linear electro-optic coefficient, E is the electric field, $S_{11,12}$ is the quadratic coefficient for TM and TE polarization, N_d is the doping level of the carrier concentration, e is the electron charge, ε_0 is the vacuum permittivity, c is the light speed in vacuum, m_{hh} and m_{lh} are the heavy and light hole masses, respectively, P and N are the electron and hole concentrations, respectively, m_e is the electron mass, and λ is the wavelength. The main parameters of the electro-optic effects are listed in Table 1.

The semiconductor and Maxwell's equations were taken into account using COMSOL software, FEM and Matlab codes to simulate the MR modulator. Spatial discretization was carried out using triangular mesh in the lateral and longitudinal cross-sections of the MR modulator.

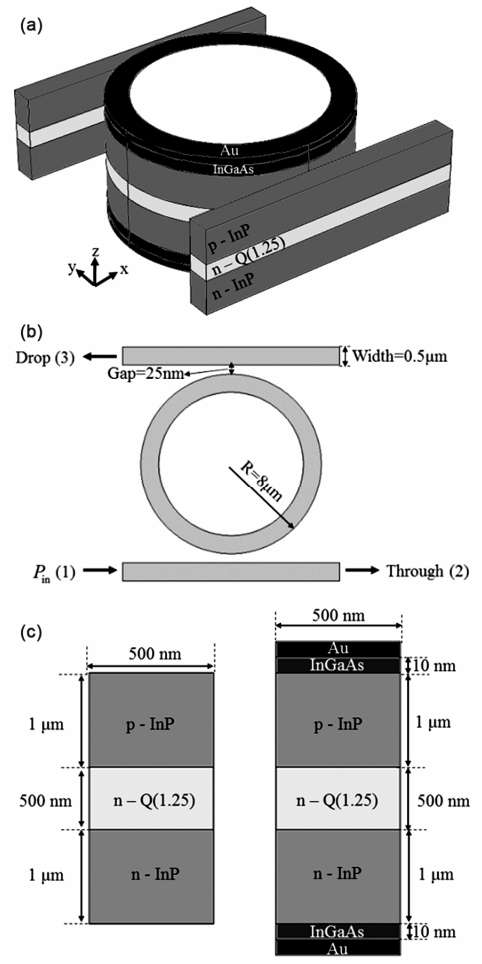

Fig. 1 – (a) Three-dimensional schematic view of the MR-modulator, (b) top view and (c) lateral cross-sections of the straight waveguide (left) and ring resonator (right) with the specifications of MR-modulator and layers

Table 1 – The main parameters of the electro-optic effect

Parameter	Value
r_{41}	1.4×10^{-12} (InP) m/V
r_{41}	1.6×10^{-12} (Q1.25) m/V
s_{12}	11.9×10^{-20} (Q1.25) m^2/V^2
s_{11}	21.5×10^{-20} (Q1.25) m^2/V^2
$A(E)$	3.65×10^{-27} (InP) m^3
$A(E)$	5.7×10^{-27} (Q1.25) m^3
A_{BF}	5×10^{-21} (InP) m^3
A_{BF}	14×10^{-21} (Q1.25) m^3
n_{InP}	3.1669
$n_{Q(1.25)}$	3.3636

In the first step, electrical simulation was done by solving the continuity, Poisson's, and impact ionization equations for each biasing voltage to determine all relevant quantities, including carrier distribution and electrical field in the lateral cross-section of the microring (Figs 2 and 3).

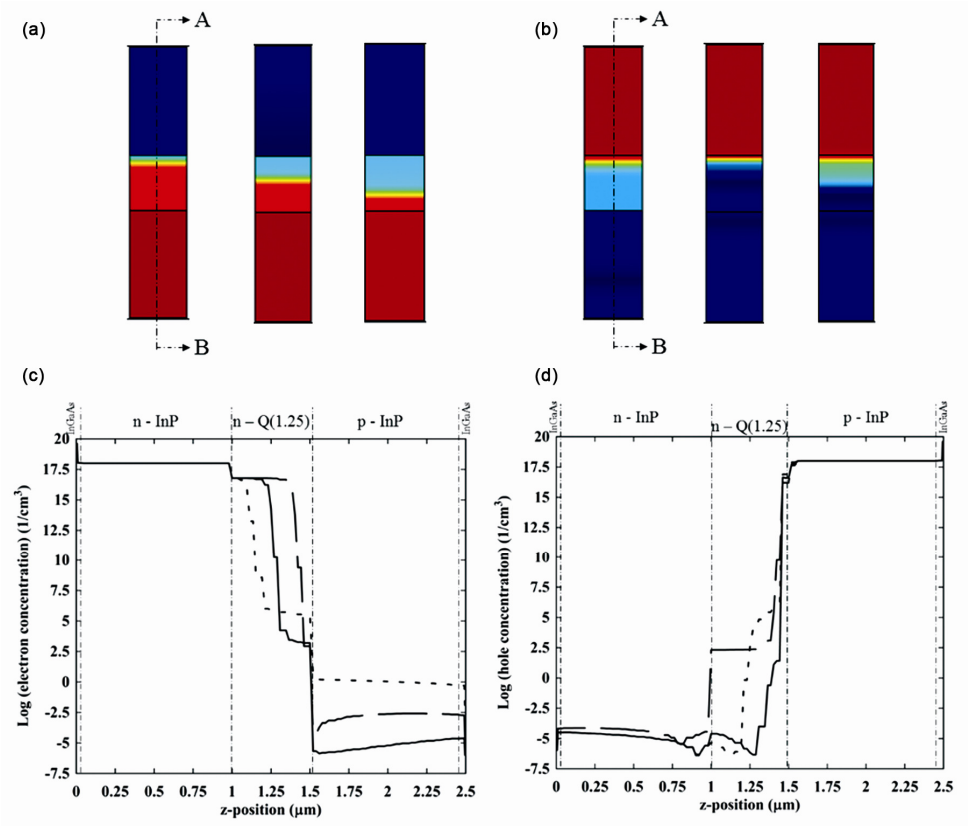

Fig. 2 – (a) Electrons, (b) holes concentrations at 0, -3, and -7 V (from left to right), (c) electrons and (d) holes concentrations at A-B cross-sections for 0 V (– –), -3 V (——), and -7 V (···)

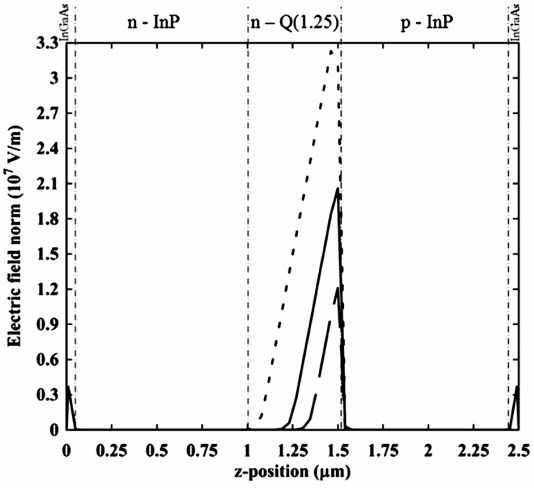

Fig. 3 – Electric field distribution at the three bias voltages of 0 V (– –), -3 V

As expected, the depletion region extended toward the whole InGaAsP layer and the electrical field was increased by increasing the reverse voltage applied to the electrodes. The variations in refractive index (Δn_{total}) were calculated using relations (1-5) in all mesh nodes. The effective refractive index of the ring resonator, determined by modal analysis as a function of the biasing voltage, is shown in Fig. 4. The effective refractive index declined linearly with the reverse increase in the biasing voltage. The effective refractive index of the straight waveguide was calculated to be 3.05171 for TE polarization. In the second step, the optical continuous wave was launched to the input port of the longitudinal cross-section of the ring resonator shown in Fig. 1(b). The optical powers transmitted to the through and drop ports of the MR modulator were determined by solving the Maxwell's equations. The magnitude of the optical power transmitted to the through port ($|S_{21}|$) as a function of the incident optical wavelength is shown in Fig. 5 at a biasing voltage of 0 V. This demonstrated a resonance peak at a wavelength of 1.56142 µm, a free spectral range of 16.1 nm and a full width at half maximum of 2.01 nm. By applying bias voltages of -3 and -7 V, the resonance wavelength peaks shift 0.33 and 0.77 nm, which results in 43 and 50 dB extinction ratios, respectively (Fig 6). The magnitude of the optical output power (($|S_{21}|$) versus the voltages applied to the through port is shown in Fig. 7 at an incident optical wavelength of 1.56066 µm and demonstrated linear behaviour like that of the effective refractive index of the ring.

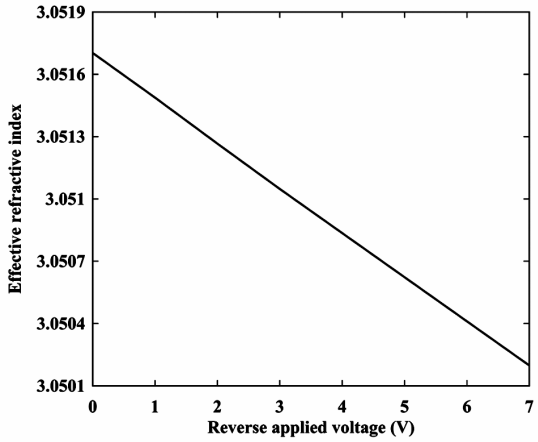

Fig. 4 – Effective refractive index of ring as a function of the biasing voltage for TE polarization mode

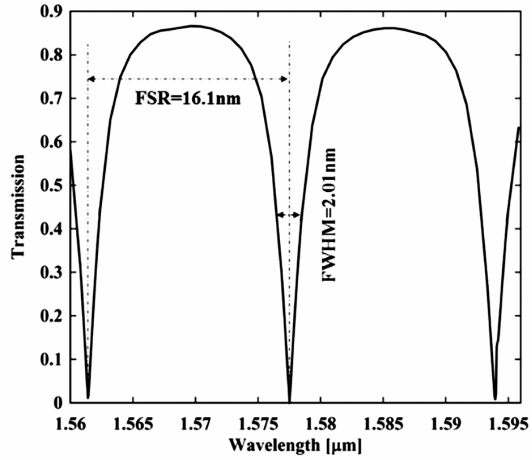

Fig. 5 – The transmission spectrum of ((|S_{21}|) MR-modulator at 0 V biasing voltage

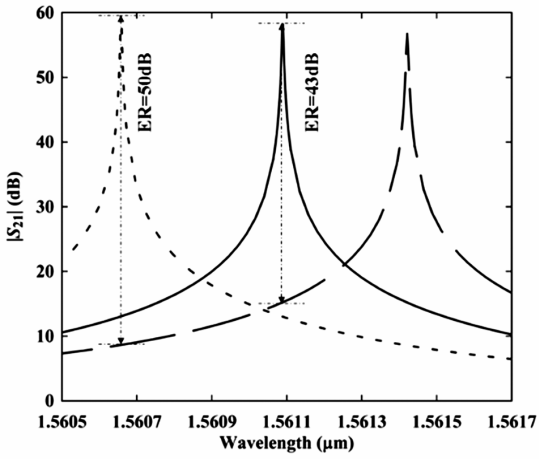

Fig. 6 – The optical transmission (|S_{21}|) as a function of wavelength at biasing voltage of 0 V (– –), -3 V (——) and -7 V (···)

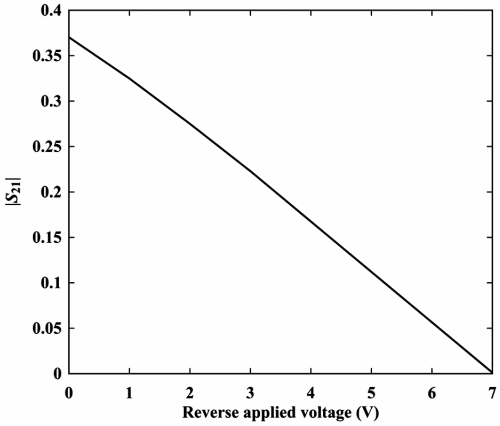

Fig. 7 – Transmission as a function of bias voltage at the wavelength peak of 1.56066 μm

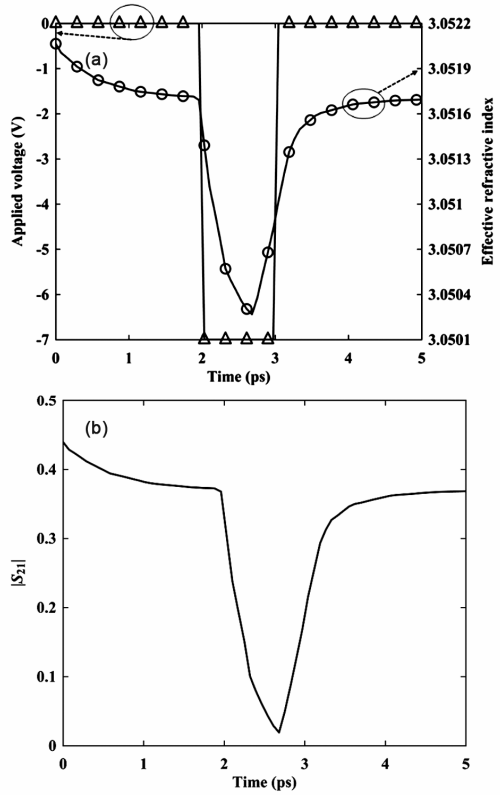

Fig. 8 – (a) The transient electric pulse (Δ) switching between two voltages of 0 and -7 V and the effective refractive index of ring (o) and (b) The optical transmission from input to through port by applying the transient electrical pulse to the electrodes

To evaluate the bandwidth of the MR-based modulator, a 1 ps transient electrical pulse ($x(t)$) was applied to the electrodes at an amplitude voltage of -7 V (Fig. 8(a)). The effective refractive index of the lateral cross-section of the ring at each applied voltage and time step was determined (Fig 8(a)). The effective refractive indices of the straight waveguide and ring were then transferred to the longitudinal cross-section. Finally, the magnitude of S_{21}

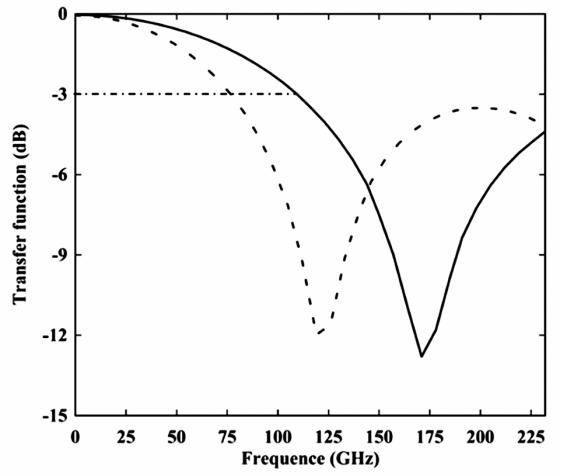

Fig. 9 – Transfer function for two applied voltages of -3 V (dot) and -7 V (solid)

was determined by illuminating an optical field with a peak resonance wavelength of 1.56066 μm at each time step, as shown in Fig. 8(b). The ratio of the fast Fourier transform (FFT) of the optical output signal ($|Y(f)| = \mathrm{FFT}(|S_{21}|)$) to the FFT of the input electrical pulse ($|X(f)| = \mathrm{FFT}(x(t))$) was calculated to determine the frequency response of the PIN modulator as $|H(f)| = |Y(f)|/|X(f)|$. Figure 9 shows the frequency response of the MR-based modulator at -3 and -7 V. It shows a 3-dB bandwidth of more than 115 GHz at the biasing voltage of -7 V.

3 Conclusions

The present study analyzed and presented a complete simulation roadmap of a high-speed microring resonator-based modulator on an InP-substrate at 1.55 μm. The modulator was simulated using FEM for DC and transient time simulations to determine the distribution of the carriers and electrical field inside the layer stacks. Variation in the effective refractive index of the ring was determined by applying reverse bias voltage caused by plasma, Pockels, Kerr, and BF effects. The reverse bias voltage shifted the resonance peak wavelength so that the optical incident signal switched back and forth between the output drop and through ports. To determine the bandwidth of the modulator, a transient voltage pulse was applied to the electrodes and the transient optical output power was calculated. The transfer function of the MR modulator was calculated using the FFT of the optical transmission to the input voltage pulse.

Acknowledgement

The Authors would like to thank to University of Kashan for supporting this work by grant no. 522827.

References

1 Hochberg M, Baehr-Jones T & Wang G, *Opt Express*, 15 (2007) 8401.
2 Koch T L & Bowers J E, *Electron Lett*, 20 (1984) 1038.
3 Su H & Lester L F, *J Phys D Appl Phys*, 38 (2005) 2112.
4 Noguchi K, Mitomi O & Miyazawa H, *J Lightwave Technol*, 16 (1998) 615.
5 Lee M, Katz H E & Erben C, *Science*, 298 (2002) 1401.
6 Khazaei H, Berolo E & Ghannouchi F, *Microwave Opt Technol Lett*, 19 (1998) 184.
7 Leclerc O, Brindel P & Rouvillain D, *Electron Lett*, 35 (1999) 730.
8 Pascher W, Den Besten J & Caprioli D, *Adv Radio Sci*, 1 (2003) 67.
9 Kikuchi N, Yamada E, Shibata Y & Ishii H, *High-Speed InP-based Mach-Zehnder modulator for advanced modulation formats*, Compound Semiconductor Integrated Circuit Symposium (CSICS) IEEE, (2012) 1.
10 De Paola F, D Alessandro V & Irace A, *Opt Commun*, 256 (2005) 326.
11 Bortnik B, Hung Y C & Tazawa H, *IEEE J Sel Top Quant*, 13 (2007) 104.
12 Xu Q, Manipatruni S & Schmidt B, *Opt Express*, 15 (2007) 430.
13 Fiedler F, Schlachetzki A, *Solid State Electron*, 30 (1987) 73.
14 Maat D H P, *InP-based integrated MZI switches for optical communication*, (TU Delft, Delft University of Technology, Netherlands), (2001) 49.